Accepted Manuscript

Topology optimization for multiscale design of porous composites with multi-domain microstructures

Jie Gao, Zhen Luo, Hao Li, Liang Gao

Please cite this article as: J. Gao, et al., Topology optimization for multiscale design of porous composites with multi-domain microstructures, *Comput. Methods Appl. Mech. Engrg.* (2018), https://doi.org/10.1016/j.cma.2018.10.017

Topology optimization for multiscale design of porous composites with multi-domain microstructures

Jie Gao [a, b], †Zhen Luo [b], Hao Li [a], *Liang Gao [a]

[a] The State Key Lab of Digital Manufacturing Equipment and Technology

Huazhong University of Science and Technology, 1037 Luoyu Road, Wuhan, Hubei 430074, China

[b] The School of Mechanical and Mechatronic Engineering

University of Technology Sydney, 15 Broadway, Ultimo, NSW 2007, Australia

† **Corresponding author:** Tel.: +61-2-95142994; E-mail: zhen.luo@uts.edu.au (A/Prof Z. Luo)

* **Corresponding author:** Tel.: +86-27-87557742; E-mail: gaoliang@mail.hust.edu.cn (Prof L. Gao)

Abstract

This paper proposes a new multiscale topology optimization method for the design of porous composites composed of the multi-domain material microstructures considering three design elements: the topology of the macrostructure, the topologies of multiple material microstructures and their overall distribution in the macrostructure. The multiscale design involves two optimization stages: the free material distribution optimization and the concurrent topology optimization. Firstly, the variable thickness sheet (VTS) method with the regularization mechanism is used to generate multiple element density distributions in the macro design domain. Hence, different groups of elements with the identical densities can be uniformly arranged in their corresponding domains, and each domain in the space will be periodically configured by a unique representative microstructure. Secondly, with the discrete material distributions achieved in the macro domain, the topology of the macrostructure and topologies of multiple representative microstructures are concurrently optimized by a parametric level set method combined with the numerical homogenization method. Finally. Several 2D and 3D numerical examples are provided to demonstrate the effectiveness of the proposed multiscale topology optimization method.

1

1 Introduction

Porous composites, comprising solids and voids, are artificially engineered to have the superior structural performances but lightweight, such as the higher specific stiffness and strength, better fatigue strength and improved corrosion-resistance [1,2] . Over the last decades, porous composites with periodically distributed microstructures have received great popularity in many engineering applications due to their easiness in manufacturing and cost effectiveness in mass production. As an example, the cellular honeycomb structures have been considerably employed in the automobile and aerospace industries [3,4]. Hence, an increasing number of analytical, numerical or experimental methods for the design of porous composites to achieve the advantage properties have been developed [1,2]. However, an efficient design method to systematically obtain the optimal layout of porous composites is still in demand.

Topology optimization [5,6] aims to seek for the best material layout in a given design domain subject to the loads and boundary conditions until the concerned performance is optimized. A wide range of methods have been developed in recent years, such as the homogenization method [7], the solid isotropic material with penalization (SIMP) [8,9], the evolutionary structural optimization (ESO) [10] and the level set method (LSM) [11−13], as well as the point wise-density interpolation (PDI) method [14,15]. Among of which, the LSM has attracted much attention in the field of structural design, due to their unique characteristics in evolving structural boundaries [12,13]. However, several complicated numerical issues are involved in the implementation of the conventional LSMs when applied to structural optimization, mainly due to the direct solution of the Hamilton-Jacobi partial differential equation (H-J PDE) [12,13], such as the extension of the boundary velocity, the re-initialization and the CFL condition.

To remove the numerical difficulties in the traditional LSMs, several variants of LSMs have been developed [16−20]. In particular, the parametric level set method (PLSM) [16,17] has been emerged as a powerful alternative approach for topology optimization, because it can not only inherit the unique characteristics of traditional LSMs, but also eliminate their numerical difficulties. The key concept of the PLSM is to interpolate the level set function by a system of the compactly supported RBFs (CSRBFs). The interpolation with compact supports greatly facilitates the application of the PLSM method to real-world optimization problems. In this way, the initial PDE-driven topological optimization is transformed into a much easier size optimization. Moreover, many well-established and gradient-based structural optimization algorithms can be directly employed, e.g. the optimality criteria (OC) [21] and the

2

method of moving asymptotes (MMA) [22]. Recently, the PLSM and its variants have been successfully applied to a range of advanced structural optimization problems [23–27].

Topology optimization has been extensively used not only in the structural design, but also in the design of cellular composite materials together with the homogenization method [28]. Sigmund [29] proposed the inverse homogenization method to design the unit cell, periodically distributed in the micro-structured materials with the prescribed constitutive parameters, as the effective properties of microstructure depend on the topology of the material microstructure rather than the intrinsic composition. After that, many different optimization methods have been developed to create a range of micro-structured composites with the tailored or extreme properties, like the extreme material properties [30,31], the maximum stiffness and fluid permeability [32,33], negative Poisson's ratio [23,34], and exotic thermomechanical properties [26]. The numerical homogenization method has been mostly used to evaluate the effective properties.

It is noted that all the above works including structures and micro-structured composites focus on the design of monoscale structures. To achieve better structural performance, the multiscale design concept has been introduced into topology optimization [35]. Currently, the multiscale topological design methods can be roughly classified into two branches. The first is developed under the assumption that the identical material microstructures are uniformly distributed in the macrostructure [36–41]. Hence, the overall macro domain is characterized with the same effective properties. The earlier work is that the identical microstructure is uniformly configured within the macrostructure subject to the macro loads and boundary conditions, while the overall topology of the macrostructure kept unchanged [39,40]. Later, the macrostructure was also topologically optimized, aligning with the optimization of the representative microstructure [37,38]. This kind of multiscale designs for porous composites can save computational time, and no connectivity issue raised because all the material microstructures are identical in size, shape and topology. However, this assumption limits the design freedom for the further improvement of the performance. The second type of methods assume that different material microstructures can exist within the macrostructure [42]. Some studies have focused on heuristic multiscale topology optimization of functionally graded materials with different types of the representative microstructures, subject to a fixed topology of the macrostructure [43–47]. After that, the multiscale topology optimization has been developed for concurrent designs of both the macro and micro topologies [48–53]. However, the computational cost is still prohibitive and manufacture is challenging, because the topologies of all

3

microstructures may demand optimization. Some works also provide the criteria for distributing multiple material microstructures in the overall macrostructure, such as a trial-and-error criterion to divide the geometrical domain [54] or the principal stress distribution [55]. However, it is noted that how to devise a uniform criterion to distribute multiple microstructures is still not available in the multiscale topology optimization. Hence, an efficient multiscale topology optimization method for composites, to consider the overall topology of the macrostructure and the topologies of different microstructures, as well as their overall distribution in the macrostructure, is still in demand.

The main motivation of this paper is to develop a new multiscale topology optimization method for the design of porous composites considering three design pillars, in order to meet both ends for the structural performance and computational efficiency. Firstly, a free material distribution optimization is developed, where the VTS method [56] is applied to generate an element-wise varied distribution of the densities and then a regularization mechanism with the defined thresholds transforms the initial distribution into a domain-wise pattern. The discrete element densities in the domain-wise pattern can determine the overall distribution of multiple representative microstructures with allowable volume fractions in the macro design domain. Then, the macrostructure and multiple material microstructures are topologically optimized in a concurrent procedure by the PLSM with the numerical homogenization method, under the overall distribution of microstructures in the macrostructure. Several numerical examples are presented to show its effectiveness of the proposed method.

4

2. Parametric level set method for porous composites

As shown in **Fig. 1**, the macrostructure contains two kinds of microstructures and each of them is periodically distributed within different regions of the macrostructure, where the global coordinate system **x** shows the macrostructure and the local coordinate system **y** denotes the microstructures. In the following, the superscript M indicates the macroscale quantities, and the m is related to the microscale quantities.
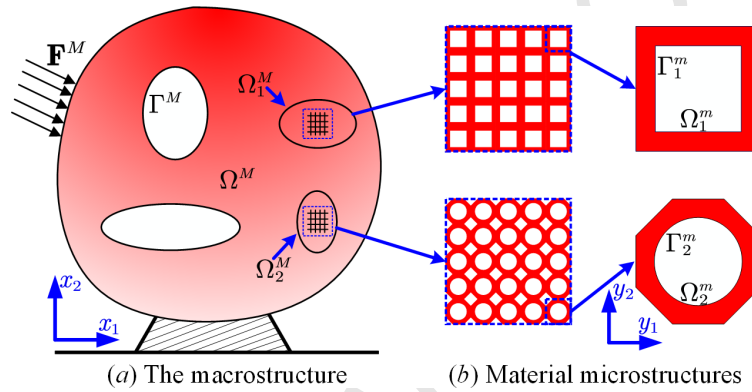

(*a*) The macrostructure   (*b*) Material microstructures
Fig. 1. Porous composites at two scales

2.1 Level set-based implicit boundary representation

In the LSM, the structural boundary is implicitly embedded into the zero-level set of a higher-dimensional level set function (LSF) [11], as shown in **Fig. 2**.

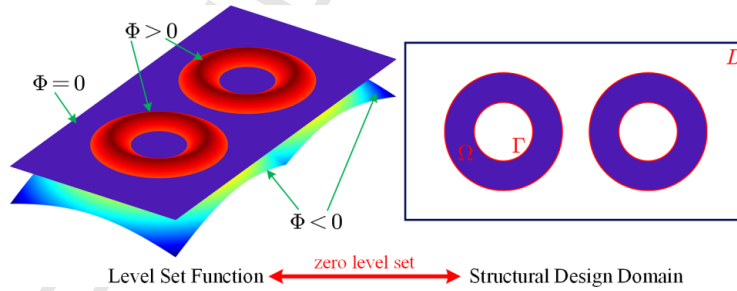**Fig. 2.** 3D LSF and 2D structural design domain

As demonstrated in **Fig. 1**, porous composites consist of a macrostructure and a number of microstructures. Hence, several LSFs should be defined to represent the topology of the macrostructure and the topologies of multiple material microstructures. Firstly, a higher-dimensional level set function for the macrostructure is expressed as follows:

5

$$\begin{cases} \Phi^M(\mathbf{x}) > 0, & \forall \mathbf{x} \in \Omega^M/\Gamma^M & (macro\ solid) \\ \Phi^M(\mathbf{x}) = 0, & \forall \mathbf{x} \in \Gamma^M \cap D^M & (macro\ boundary) \\ \Phi^M(\mathbf{x}) < 0, & \forall \mathbf{x} \in D^M/\Omega^M & (macro\ void) \end{cases} \tag{1}$$

where Ω^M, Γ^M and D^M denote the design domain, structural boundaries and the reference domain of the macrostructure, respectively. Assuming that there are a number of Θ distinct microstructures in a porous composite, the LSMs are defined for the material microstructures, respectively, as follows:

$$\begin{cases} \Phi_\xi^m(\mathbf{y}) > 0, & \forall \mathbf{y} \in \Omega_\xi^m/\Gamma_\xi^m & (micro\ solid) \\ \Phi_\xi^m(\mathbf{y}) = 0, & \forall \mathbf{y} \in \Gamma_\xi^m \cap D_\xi^m & (micro\ boundary) \quad (\xi = 1, 2, \cdots, \Theta) \\ \Phi_\xi^m(\mathbf{y}) < 0, & \forall \mathbf{y} \in D_\xi^m/\Omega_\xi^m & (micro\ void) \end{cases} \tag{2}$$

where Ω_ξ^m, Γ_ξ^m and D_ξ^m are the design domain, structural boundaries and the reference domain for the ξ_{th} representative microstructure. Introducing a pseudo-time t into Eqs. (1) and (2), both sides of them are simultaneously differentiated with respect to time variable t. The corresponding H-J PDEs at different scales can be respectively defined by

$$\begin{cases} \dfrac{\partial \Phi^M}{\partial t} - \upsilon_\mathbf{n}^M |\nabla \Phi^M| = 0 \\ \dfrac{\partial \Phi_\xi^m}{\partial t} - \upsilon_{\xi,\mathbf{n}}^m |\nabla \Phi_\xi^m| = 0 \end{cases} \tag{3}$$

where $\upsilon_\mathbf{n}^M$ and $\upsilon_{\xi,\mathbf{n}}^m$ are the corresponding normal velocity fields at two scales. Hence, the evolution of the structural topologies at two scales is governed by Eq. (3), and moving the structural boundaries by the normal velocity fields corresponds to find the solutions of the H-J PDEs. However, as mentioned previously, the direct solution of the H-J PDEs involves complicated numerical implementations [16,17], which restrains the applicability and the efficiency of the H-J PDE-driven structural optimization method.

2.2 Parameterization of the level set function

In the PLSM, the CSRBFs with C2 continuity [57] is employed here:

$$\begin{cases} \varphi_i(\mathbf{x}) = (1 - r_i(\mathbf{x}))_+^4 (4r_i(\mathbf{x}) + 1), & i = 1, 2, \cdots, N_M \\ \varphi_i(\mathbf{y}) = (1 - r_i(\mathbf{y}))_+^4 (4r_i(\mathbf{y}) + 1), & j = 1, 2, \cdots, N_m \end{cases} \tag{4}$$

where N_M is the number of the CSRBFs knots in the macrostructure, and all the representative microstructures have the same number of the CSRBFs knots N_m. r is the radius of the support domain of the basis function at the current knot, and the detailed information at different scales is given as:

6

$$\begin{cases} r_i(\mathbf{x}) = \dfrac{\|\mathbf{x} - \mathbf{x}_i\|}{d_M} \\ r_i(\mathbf{y}) = \dfrac{\|\mathbf{y} - \mathbf{y}_i\|}{d_m} \end{cases} \tag{5}$$

where d_M controls the scale of the support domain at the macrostructure, and d_m is the corresponding term in the microstructures. Then, the time-dependent LSFs are interpolated by a given set of CSRBFs that are fixed in the space and their expansion coefficients by

$$\begin{cases} \Phi^M(\mathbf{x},t) = \boldsymbol{\varphi}^T(\mathbf{x})\boldsymbol{\alpha}^M(t) = \displaystyle\sum_{i=1}^{N_M} \varphi_i(\mathbf{x})\alpha_i^M(t) \\ \Phi_\xi^m(\mathbf{y},t) = \boldsymbol{\varphi}^T(\mathbf{y})\boldsymbol{\alpha}_\xi^m(t) = \displaystyle\sum_{i=1}^{N_m} \varphi_i(\mathbf{y})\alpha_{\xi,i}^m(t) \end{cases} \tag{6}$$

The series of CSRBFs are formulated as a vector at every knot:

$$\begin{cases} \boldsymbol{\varphi}(\mathbf{x}) = \begin{bmatrix} \varphi_1(\mathbf{x}) & \varphi_2(\mathbf{x}) & \cdots & \varphi_{N_M}(\mathbf{x}) \end{bmatrix} \\ \boldsymbol{\varphi}(\mathbf{y}) = \begin{bmatrix} \varphi_1(\mathbf{y}) & \varphi_2(\mathbf{y}) & \cdots & \varphi_{N_m}(\mathbf{y}) \end{bmatrix} \end{cases} \tag{7}$$

The expansion coefficients are expressed in the same manner, as follows:

$$\begin{cases} \boldsymbol{\alpha}^M(t) = \begin{bmatrix} \alpha_1^M(t) & \alpha_2^M(t) & \cdots & \alpha_{N_M}^M(t) \end{bmatrix} \\ \boldsymbol{\alpha}_\xi^m(t) = \begin{bmatrix} \alpha_{\xi,1}^m(t) & \alpha_{\xi,2}^m(t) & \cdots & \alpha_{\xi,N_m}^m(t) \end{bmatrix} \end{cases} \tag{8}$$

Once time and space are decoupled by the above interpolation, the term of CSRBFs $\boldsymbol{\varphi}$ is only dependent on space, and the term of expansion coefficient $\boldsymbol{\alpha}$ is only dependent on time. Substituting Eq. (6) into Eq. (3), the H-J PDEs are transformed into the time-space independent forms as:

$$\begin{cases} \boldsymbol{\varphi}^T(\mathbf{x}) \dfrac{d\boldsymbol{\alpha}^M(t)}{dt} - \upsilon_\mathbf{n}^M |\nabla \boldsymbol{\varphi}^T(\mathbf{x})\boldsymbol{\alpha}^M(t)| = 0 \\ \boldsymbol{\varphi}^T(\mathbf{y}) \dfrac{d\boldsymbol{\alpha}_\xi^m(t)}{dt} - \upsilon_{\xi,\mathbf{n}}^m |\nabla \boldsymbol{\varphi}^T(\mathbf{y})\boldsymbol{\alpha}_\xi^m(t)| = 0 \end{cases} \tag{9}$$

Then, the normal velocities $\upsilon_\mathbf{n}^M$ and $\upsilon_{\xi,\mathbf{n}}^m$ at two scales can be given by:

$$\begin{cases} \upsilon_\mathbf{n}^M = \dfrac{\boldsymbol{\varphi}^T(\mathbf{x})}{|\nabla \boldsymbol{\varphi}^T(\mathbf{x})\boldsymbol{\alpha}^M(t)|} \dfrac{d\boldsymbol{\alpha}^M(t)}{dt} \\ \upsilon_{\xi,\mathbf{n}}^m = \dfrac{\boldsymbol{\varphi}^T(\mathbf{y})}{|\nabla \boldsymbol{\varphi}^T(\mathbf{y})\boldsymbol{\alpha}_\xi^m(t)|} \dfrac{d\boldsymbol{\alpha}_\xi^m(t)}{dt} \end{cases} \tag{10}$$

In Eq. (10), it can be seen that the normal velocity fields have been naturally extended to the whole design domain at two scales due to the definition of the CSRBFs over the whole design domain. The H-J PDEs

7

at two scales have been converted into two new forms, respectively, where the ordinary differential equations (ODEs) are defined with a set of unknown expansion coefficients serving as the design variables.

3 Multiscale topology optimization for porous composites

The core idea of the multiscale topology optimization method for porous composites has been clearly illustrated in **Fig. 3**. The whole procedure can be involved into two stages: the free material distribution optimization and the concurrent optimization considering three design pillars in porous composites. As an example of a cantilever beam, the initial structure is defined in **Fig. 3** (*a*).
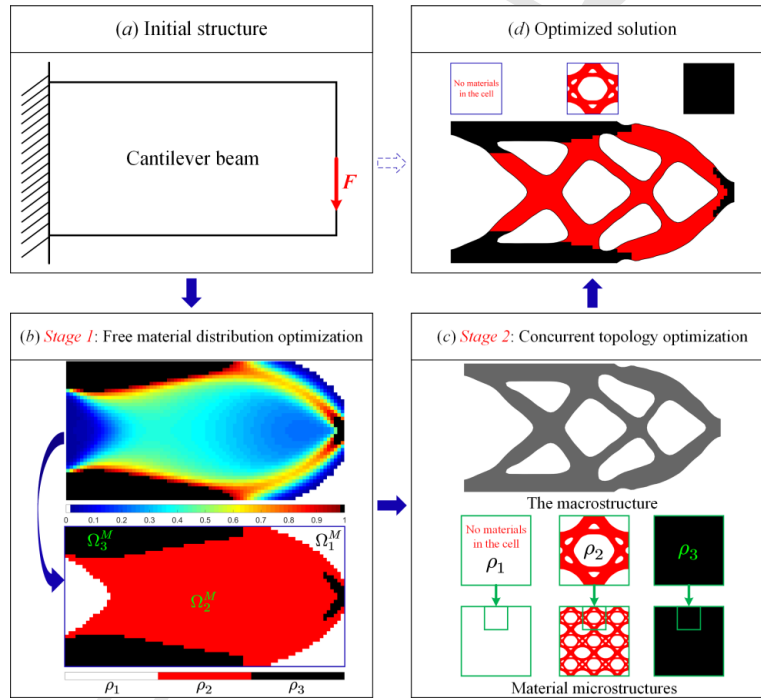

Fig. 3. Multiscale topology optimization of porous composites

At the stage 1, the VTS [56] method is firstly applied to generate the element densities which are distributed in an element-wise pattern, as illustrated in the first plot of **Fig. 3** (*b*). It can be seen that the optimized macro design domain comprises a large number of the intermediate element densities, which can lead to interpretations of a huge amount of microstructures to be designed. Hence, the continuous distribution makes the latter concurrent optimization computationally prohibitive. Here we introduce a regularization mechanism to discretize the continuous density distribution, to reduce the number of the intermediate densities. The elements with the same or proximal densities will be classified into the same

group. Then, the average of the element densities within each group is utilized to represent the density of this group. The re-distribution of the regularized element densities is displayed in the second plot of **Fig. 3** (*b*). It can be seen that the regularized element densities are distributed in a domain-wise pattern. Each sub domain is only characterized by one equivalent density.

After that, the regularized density in each region will be chosen as the maximum volume fraction for the corresponding microstructure. Only one representative microstructure will be topologically optimized and periodically arranged within each region. Hence, it can be confirmed that the distribution of the regularized element densities corresponds to the overall distribution of multiple representative microstructures with the allowable volume fractions to be designed in the macrostructure. The topology of the macrostructure and the topologies of multiple representative microstructures are concurrently optimized in the stage 2, subject to the overall distribution of multiple microstructures in the stage 1. At the macro scale, the PLSM is applied to optimize the topology of the macrostructure under the global volume constraint. Meanwhile, at the micro scale, the topology of each representative microstructure is also optimized by the PLSM integrated with the numerical homogenization method, under the corresponding volume constraint defined by the regularized element density. As displayed in **Fig. 3** (*c*), the optimized topologies of the macrostructure and three representative microstructures are provided. The final multiscale design of the cantilever beam is also displayed in **Fig. 3** (*d*), where the macro topology comprises three sub domains plotted with the white, red and black colors, respectively. Each sub domain within the optimized macrostructure is uniformly configured by the corresponding representative microstructure with the same color.

In conclusion, free material distribution optimization determines the number and overall distribution pattern of the representative microstructures to be designed within the macrostructure, while the topologies of both the macrostructure and the macrostructure are optimized in the concurrent optimization stage.

3.1 Free material distribution optimization

3.1.1 VTS method

In the free material distribution optimization, the formulation using the VTS method is written as:

9

$$\begin{cases} Find\colon \ \boldsymbol{\rho} = \left\{\rho_1, \ \rho_2, \ \cdots, \ \rho_{N_e}\right\} \\[2mm] Min\colon \ J = \mathbf{F}^T \mathbf{U} = \mathbf{U}^T \mathbf{K}^T \mathbf{U} = \sum_{e=1}^{N_e} \rho_e \mathbf{U}_e^T \mathbf{K}_0 \mathbf{U}_e \\[2mm] S.t\colon \ \begin{cases} \mathbf{K}\mathbf{U} = \mathbf{F} \\[1mm] G_d = \sum_{e=1}^{N_e} \rho_e \upsilon_0 - V_d \leqslant 0 \\[1mm] 0 < \rho_{\min} \leqslant \rho_e \leqslant 1, \ (e = 1, 2, \cdots, N_e) \end{cases} \end{cases} \qquad (11)$$

where $\boldsymbol{\rho}$ is the vector of the design variables, also the element densities, and $\rho_{\min}$ is the minimum of the element densities to avoid the numerical singularity. N_e is the total number of the design elements. J is the structural compliance. $\mathbf{F}$ and $\mathbf{U}$ are the external load vector and the global displacement vector, respectively. $\mathbf{K}$ is the global stiffness matrix, and $\mathbf{K}_0$ is the stiffness matrix of the solid element. $\mathbf{U}_e$ is the displacement vector in the ρ_e element. G_d is the volume constraint, where V_d is the allowable volume fraction and υ_0 is the solid volume fraction of the solid element.

3.1.2 The regularization mechanism

Assuming that the densities in the initial distribution are classified into Θ groups (also the number of distinct material microstructures), the regularized mechanism is defined as:

$$\overline{\rho}_\xi = \frac{1}{N_\xi} \sum_{i=1}^{N_\xi} \rho_\xi^i \quad (\rho_\xi^{min} \leqslant \rho_\xi^i < \rho_\xi^{max}, \ \xi = 1, 2, \cdots, \Theta) \qquad (12)$$

where ρ_ξ^i is the i_{th} element density in the ξ_{th} group. The ρ_ξ^{min} and ρ_ξ^{max} indicate the lower and upper thresholds for the element densities in the ξ_{th} group, respectively. N_ξ is the total number of the elements in the ξ_{th} group, and $\overline{\rho}_\xi$ is the regularized density of the ξ_{th} group which is defined by the mean value of all the element densities in this group. Hence, the whole macro design domain is divided into Θ sub domains, and each of them is homogeneously occupied by one equivalent element density.

3.2 Concurrent topology optimization

The concurrent topology optimization for the macrostructure and multiple representative microstructures to minimize the structural static compliance is developed by the PLSM with the numerical homogenization method, subject to the overall distribution of the multiple microstructures, given as:

10

$$
\begin{cases}
\textit{Find: } \alpha_i^M, \ \alpha_{\xi,j}^m \ \ (i=1,2,\cdots,N_M; \ \xi=1,2,\cdots,\Theta; \ j=1,2,\cdots,N_m) \\[2mm]
\underset{\mathbf{u},\Phi}{\textit{Min: }} J(\mathbf{u},\Phi) = \sum_{\xi=1}^{\Theta} \int_{D^M} \boldsymbol{\varepsilon}(\mathbf{u}_\xi^M) \mathbf{D}_\xi^H(\mathbf{u}_\xi^m,\Phi_\xi^m) \boldsymbol{\varepsilon}(\mathbf{u}_\xi^M) H(\Phi_\xi^M) d\Omega^M \\[2mm]
\textit{S.t: }
\begin{cases}
a(\Phi^M,\mathbf{u}^M,\mathbf{v}^M,\mathbf{D}^H) = l(\Phi^M,\mathbf{v}^M), \qquad \forall \mathbf{v}^M \in \bar{\mathrm{U}}(\Omega^M) \\[2mm]
a(\Phi_\xi^m,\mathbf{u}_\xi^m,\mathbf{v}_\xi^m) = l(\Phi_\xi^m,\mathbf{v}_\xi^m), \qquad \forall \mathbf{v}_\xi^m \in \bar{\mathrm{U}}(\Omega_\xi^m) \\[2mm]
G_M = \sum_{\xi=1}^{\Theta} \left\{ \left(\int_{D^M} H(\Phi_\xi^M) d\Omega^M \right) \left(\int_{D_\xi^m} H(\Phi_\xi^m) d\Omega_\xi^m \right) \right\} - V_M \leqslant 0 \\[2mm]
G_\xi^m = \int_{D_\xi^m} H(\Phi_\xi^m) d\Omega_\xi^m - \overline{\rho}_\xi \leqslant 0 \\[2mm]
\alpha_{min}^M \leqslant \alpha_i^M \leqslant \alpha_{max}^M; \ \ \alpha_{\xi,min}^m \leqslant \alpha_{\xi,j}^m \leqslant \alpha_{\xi,max}^m
\end{cases}
\end{cases}
\tag{13}
$$

where α_i^M is the i_{th} macro design variable bounded by α_{min}^M and α_{max}^M. $\alpha_{\xi,min}^m$ and $\alpha_{\xi,max}^m$ are the corresponding lower and upper bounds of the design variable $\alpha_{\xi,j}^m$ for the ξ_{th} material representative microstructure. J is the objective function defined by the structural compliance. G_M is the total material volume constraint, which is calculated considering the macrostructure and its microstructures. V_M is the allowable volume fraction for the global volume constraint. G_ξ^m is the volume constraint for the ξ_{th} representative material microstructure, which is subject to the maximum volume fraction defined by the regularized density $\overline{\rho}_\xi$ in the free material distribution optimization. H is the Heaviside function [12,13]. $\mathbf{u}^M$ is the displacement field of the macrostructure. $\mathbf{v}^M$ is the macro virtual displacement field belonging to the kinematically admissible space $\bar{\mathrm{U}}(\Omega^M)$.

The equilibrium equation is developed by the principle of virtual work, where the bilinear energy term a and the linear load term l are given by:

$$
\begin{cases}
a(\Phi^M,\mathbf{u}^M,\mathbf{v}^M,\mathbf{D}^H) = \sum_{\xi=1}^{\Theta} \int_{D^M} \boldsymbol{\varepsilon}(\mathbf{u}_\xi^M) \mathbf{D}_\xi^H(\mathbf{u}_\xi^m,\Phi_\xi^m) \boldsymbol{\varepsilon}(\mathbf{v}_\xi^M) H(\Phi_\xi^M) d\Omega^M \\[2mm]
l(\Phi^M,\mathbf{v}^M) = \int_{D^M} \mathbf{p}^M \mathbf{v}^M H(\Phi^M) d\Omega^M + \int_{D^M} \mathbf{F}^M \mathbf{v}^M \delta(\Phi^M) |\nabla \Phi^M| d\Omega^M
\end{cases}
\tag{14}
$$

where $\mathbf{p}^M$ is the macro body force, and $\mathbf{F}^M$ is the macro boundary traction. δ is the partial derivative of the Heaviside function, namely the Dirac function [58]. The homogenized effective elastic tensor $\mathbf{D}_\xi^H$ of the ξ_{th} representative microstructure is evaluated by the numerical homogenization method [28], as:

$$
D_{\xi(ijkl)}^H = \frac{1}{|\Omega_\xi^m|} \int_{D_\xi^m} \left(\varepsilon_{pq}^{0(ij)} - \varepsilon_{pq}^*(u_\xi^{m(ij)}) \right) D_{pqrs} \left(\varepsilon_{rs}^{0(kl)} - \varepsilon_{rs}^*(u_\xi^{m(kl)}) \right) H(\Phi_\xi^m) d\Omega_\xi^m
\tag{15}
$$

where $|\Omega_\xi^m|$ is the area in 2D or the volume in 3D of the ξ_{th} representative microstructure, and D_{pqrs} is the elasticity property of the solid material. ε_{pq}^0 is the initial unit test strain field, which contains three

11

or six unit vectors in 2D or 3D [29]. ε_{pq}^{*} is the locally varying strain field induced by ε_{pq}^{0}. The unknown displacement $u_{\xi}^{m(ij)}$ is calculated by the micro equilibrium equation under the initial unit test strain $\varepsilon_{pq}^{0(ij)}$.

The weak forms for both the energy a and load l terms for the ξ_{th} representative material microstructure are defined as, respectively:

$$\begin{cases} a(\Phi_{\xi}^{m}, \mathbf{u}_{\xi}^{m}, \mathbf{v}_{\xi}^{m}) = \int_{D_{\xi}^{m}} \varepsilon_{pq}^{*}(u_{\xi}^{m(ij)}) D_{pqrs} \varepsilon_{rs}^{*}(v_{\xi}^{m(kl)}) H(\Phi_{\xi}^{m}) d\Omega_{\xi}^{m} \\ l(\Phi_{\xi}^{m}, \mathbf{v}_{\xi}^{m}) = \int_{D_{\xi}^{m}} \varepsilon_{pq}^{0(ij)} D_{pqrs} \varepsilon_{rs}^{*}(v_{\xi}^{m(kl)}) H(\Phi_{\xi}^{m}) d\Omega_{\xi}^{m} \end{cases} \tag{16}$$

where $v_{\xi}^{m(ij)}$ is the micro virtual displacement field of the ξ_{th} representative microstructure belonging to the micro kinematically admissible displacement space $\overline{U}(\Omega_{\xi}^{m})$.

4 Design sensitivity analysis

In the proposed multiscale topology optimization, both the VTS and PLSM employed in the problems can be solved by many well-established optimization algorithms [21,22]. Hence, the sensitivity information of the objective and constraint functions are required. In the above optimization formulation, three kinds of design variables are existed, including the element densities in the free material distribution optimization, the expansion coefficients for macro and micro structures in the concurrent optimization.

4.1 Sensitivity analysis in the free material distribution optimization

In the VTS, the first-order derivatives of the objective with respect to the element densities are computed by using the adjoint variable method [59], stated as:

$$\frac{\partial J}{\partial \rho_e} = -\mathbf{U}^T \frac{\partial \mathbf{K}^T}{\partial \rho_e} \mathbf{U} = -\mathbf{U}_e^T \mathbf{K}_0 \mathbf{U}_e \tag{17}$$

Besides, the derivatives of the volume constraint are given by:

$$\frac{\partial G_d}{\partial \rho_e} = \partial \left(\sum_{e=1}^{N_e} \rho_e v_0 - V_d \right) \Big/ \partial \rho_e = v_0 \tag{18}$$

4.2 Macro sensitivity analysis in the concurrent optimization

12

Here, a Lagrangian function L for the constrained problem in Eq. (13) is defined. The volume constraints at the micro are not considered because they are independent on the macro design variables, given as:

$$L(\mathbf{u},\Phi) = J(\mathbf{u},\Phi) + l(\Phi^M,\mathbf{v}^M) - a(\Phi^M,\mathbf{u}^M,\mathbf{v}^M,\mathbf{D}^H) + \lambda_0 G_M \tag{19}$$

The shape derivative of the Lagrangian function is derived by the shape sensitivity analysis [58] as:

$$\frac{dL(\mathbf{u},\Phi)}{dt} = \int_{D^M} \beta(\mathbf{u},\Phi,\mathbf{D}^H) \upsilon_{\mathbf{n}}^M \delta(\Phi^M) |\nabla\Phi^M| d\Omega^M = \int_{\Gamma^M} \beta(\mathbf{u},\Phi,\mathbf{D}^H) \upsilon_{\mathbf{n}}^M d\Gamma^M \tag{20}$$

where

$$\beta = -\sum_{\xi=1}^{\Theta} \boldsymbol{\varepsilon}(\mathbf{u}_{\xi}^M) \mathbf{D}_{\xi}^H \boldsymbol{\varepsilon}(\mathbf{u}_{\xi}^M) + 2[\mathbf{p}^M\mathbf{u}^M + \nabla(\mathbf{F}^M\mathbf{u}^M)\cdot\mathbf{n} + \kappa(\mathbf{F}^M\mathbf{u}^M)] + \lambda_0\left(\sum_{\xi=1}^{\Theta}\int_{D_{\xi}^m} H(\Phi_{\xi}^m)d\Omega_{\xi}^m\right) \tag{21}$$

and κ is the mean curvature in two dimensions [12,16,17]. Now, recalling the normal velocity field $\upsilon_{\mathbf{n}}^M$ in Eq. (10) and substituting it into Eq. (21), and the shape derivative of the Lagrangian function L can be written as:

$$\frac{dL(\mathbf{u},\Phi)}{dt} = \int_{\Gamma^M} \left(\beta(\mathbf{u},\Phi,\mathbf{D}^H)\frac{\boldsymbol{\varphi}^T(\mathbf{x})}{|\nabla\boldsymbol{\varphi}^T(\mathbf{x})\boldsymbol{\alpha}^M(t)|}\right) \frac{d\boldsymbol{\alpha}^M(t)}{dt} d\Gamma^M \tag{22}$$

Eq. (22) can be expanded as:

$$\frac{dL(\mathbf{u},\Phi)}{dt} = \mathcal{P}^T \frac{d\boldsymbol{\alpha}^M(t)}{dt} + \mathcal{Q}^T \frac{d\boldsymbol{\alpha}^M(t)}{dt} \tag{23}$$

where $\mathcal{P}^T$ and $\mathcal{Q}^T$ are defined as:

$$\begin{cases} \mathcal{P}^T = \int_{\Gamma^M} \beta_1(\mathbf{u},\Phi,\mathbf{D}^H)\dfrac{\boldsymbol{\varphi}^T(\mathbf{x})}{|\nabla\boldsymbol{\varphi}^T(\mathbf{x})\boldsymbol{\alpha}^M(t)|}d\Gamma^M \\ \mathcal{Q}^T = \lambda_0\left(\displaystyle\sum_{\xi=1}^{\Theta}\int_{D_{\xi}^m} H(\Phi_{\xi}^m)d\Omega_{\xi}^m\right)\int_{\Gamma^M}\dfrac{\boldsymbol{\varphi}^T(\mathbf{x})}{|\nabla\boldsymbol{\varphi}^T(\mathbf{x})\boldsymbol{\alpha}^M(t)|}d\Gamma^M \end{cases} \tag{24}$$

where

$$\beta_1 = -\sum_{\xi=1}^{\Theta} \boldsymbol{\varepsilon}(\mathbf{u}_{\xi}^M)\mathbf{D}_{\xi}^H(\mathbf{u}_{\xi}^m,\Phi_{\xi}^m)\boldsymbol{\varepsilon}(\mathbf{u}_{\xi}^M) + 2[\mathbf{p}^M\mathbf{u}^M + \nabla(\mathbf{F}^M\mathbf{u}^M)\cdot\mathbf{n} + \kappa(\mathbf{F}^M\mathbf{u}^M)] \tag{25}$$

On the other side, the shape derivative of the Lagrangian function L can be gained based on the chain rule.

13

$$\frac{dL(\mathbf{u},\Phi)}{dt} = \left(\frac{\partial J(\mathbf{u},\Phi)}{\partial \boldsymbol{\alpha}^M} + \lambda_0 \frac{\partial G_M}{\partial \boldsymbol{\alpha}^M}\right)\frac{d\boldsymbol{\alpha}^M(t)}{dt} \tag{26}$$

Thus, the design sensitivities of the objective and constraint functions with respect to the expansion coefficients at macro scale are obtained by comparing the corresponding terms in Eqs. (24) and (26):

$$\begin{cases} \dfrac{\partial J(\mathbf{u},\Phi)}{\partial \boldsymbol{\alpha}^M} = \displaystyle\int_{\Gamma^M} \beta_1(\mathbf{u},\Phi,\mathbf{D}^H)\dfrac{\boldsymbol{\varphi}^T(\mathbf{x})}{|\nabla\boldsymbol{\varphi}^T(\mathbf{x})\boldsymbol{\alpha}^M(t)|}d\Gamma^M \\ \dfrac{\partial G_M}{\partial \boldsymbol{\alpha}^M} = \left(\displaystyle\sum_{\xi=1}^{\Theta}\displaystyle\int_{D_\xi^m}H(\Phi_\xi^m)d\Omega_\xi^m\right)\displaystyle\int_{\Gamma^M}\dfrac{\boldsymbol{\varphi}^T(\mathbf{x})}{|\nabla\boldsymbol{\varphi}^T(\mathbf{x})\boldsymbol{\alpha}^M(t)|}d\Gamma^M \end{cases} \tag{27}$$

In order to improve the numerical efficiency of the optimization, the design sensitivities expressed by the boundary integration scheme are transformed into the following volume integration [16,24], given as.

$$\begin{cases} \dfrac{\partial J(\mathbf{u},\Phi)}{\partial \boldsymbol{\alpha}^M} = \displaystyle\int_{D^M} \beta_1(\mathbf{u},\Phi,\mathbf{D}^H)\boldsymbol{\varphi}^T(\mathbf{x})\delta(\Phi^M)d\Omega^M \\ \dfrac{\partial G_M}{\partial \boldsymbol{\alpha}^M} = \left(\displaystyle\sum_{\xi=1}^{\Theta}\displaystyle\int_{D_\xi^m}H(\Phi_\xi^m)d\Omega_\xi^m\right)\displaystyle\int_{D^M}\boldsymbol{\varphi}^T(\mathbf{x})\delta(\Phi^M)d\Omega^M \end{cases} \tag{28}$$

4.3 Micro sensitivity analysis in the concurrent optimization

Here, the first-order derivatives of the objective and constraint functions with respect to the micro design variables (the micro expansion coefficients) are computed based on the chain rule, given by:

$$\frac{\partial J(\mathbf{u},\Phi)}{\partial \boldsymbol{\alpha}_\xi^m} = \int_{D^M} \boldsymbol{\varepsilon}(\mathbf{u}_\xi^M)\frac{\partial \mathbf{D}_\xi^H}{\partial \boldsymbol{\alpha}_\xi^m}\boldsymbol{\varepsilon}(\mathbf{u}_\xi^M)H(\Phi_\xi^M)d\Omega^M \tag{29}$$

It can be found that the key to calculate the sensitivities in Eq. (29) is the derivative of $\mathbf{D}_\xi^H$ with respect to the micro design variable, which can be derived via the shape derivative [23,58], given as:

$$\frac{\partial D_{\xi(ijkl)}^H}{\partial t} = \frac{1}{|\Omega_\xi^m|}\int_{D_\xi^m}\left(\varepsilon_{pq}^{0(ij)} - \varepsilon_{pq}^*\left(u_\xi^{m(ij)}\right)\right)D_{pqrs}\left(\varepsilon_{rs}^{0(kl)} - \varepsilon_{rs}^*\left(u_\xi^{m(kl)}\right)\right)\upsilon_{\xi,\mathbf{n}}^m\delta(\Phi_\xi^m)|\nabla\Phi_\xi^m|d\Omega_\xi^m \tag{30}$$

Recalling the micro normal velocity field $\upsilon_{\xi,\mathbf{n}}^m$ in Eq. (10), and substituting it into Eq. (30) will yield:

$$\frac{\partial D_{\xi(ijkl)}^H}{\partial t} = \left(\frac{1}{|\Omega_\xi^m|}\int_{D_\xi^m}\left(\varepsilon_{pq}^{0(ij)} - \varepsilon_{pq}^*\left(u_\xi^{m(ij)}\right)\right)D_{pqrs}\left(\varepsilon_{rs}^{0(kl)} - \varepsilon_{rs}^*\left(u_\xi^{m(kl)}\right)\right)\boldsymbol{\varphi}^T(\mathbf{y})\delta(\Phi_\xi^m)d\Omega_\xi^m\right)\frac{d\boldsymbol{\alpha}_\xi^m(t)}{dt} \tag{31}$$

Based on the chain rule, the first-order derivative of $\mathbf{D}_\xi^H$ with respect to time *t* is given by:

$$\frac{\partial D_{\xi(ijkl)}^H}{\partial t} = \frac{\partial D_{\xi(ijkl)}^H}{\partial \boldsymbol{\alpha}_\xi^m}\frac{\partial \boldsymbol{\alpha}_\xi^m(t)}{\partial t} \tag{32}$$

14

According to the Eqs. (30) and (31), it can be found that the first-order derivative of $\mathbf{D}_\xi^H$ with respect to the micro expansion coefficient can be given as:

$$\frac{\partial D_{\xi(ijkl)}^H}{\partial \boldsymbol{\alpha}_\xi^m} = \frac{1}{|\Omega_\xi^m|} \int_{D_\xi^m} \left(\varepsilon_{pq}^{0(ij)} - \varepsilon_{pq}^\star \left(u_\xi^{m(ij)} \right) \right) D_{pqrs} \left(\varepsilon_{rs}^{0(kl)} - \varepsilon_{rs}^\star \left(u_\xi^{m(kl)} \right) \right) \boldsymbol{\varphi}^T(\mathbf{y}) \delta(\Phi_\xi^m) d\Omega_\xi^m \qquad (33)$$

Finally, the first-order derivatives of the objective function with respect to micro design variables can be attained by substituting Eq. (33) into Eq. (29). Similarly, the first-order derivative of the volume constraint with respect to the micro design variable is given as:

$$\frac{\partial G_\xi^m}{\partial \boldsymbol{\alpha}_\xi^m} = \int_{D_\xi^m} \boldsymbol{\varphi}^T(\mathbf{y}) \delta(\Phi_\xi^m) d\Omega_\xi^m \qquad (34)$$

5 Numerical implementations

Here, the OC algorithm [21] is used to update the design variables in the multiscale design. The details for updating mechanism in the OC method can refer to [17]. The flowchart of the proposed multiscale topology optimization method is shown in **Fig. 4**. The first stage aims to seek for the appropriate distribution of the representative material microstructures with allowable volume fractions in the macrostructure by the VTS method combined with the regularization mechanism in Eqs. (11) and (12). With the overall distribution of multiple representative material microstructures, the concurrent optimization of the macro and micro topologies is performed by the PLSM integrated with the numerical homogenization method in Eq. (13). The design sensitivities for the free material distribution optimization and the concurrent optimization are respectively evaluated by Eqs. (17), (18), (28), (33) and (34). The optimization is terminated until the criterion for the convergence is met.
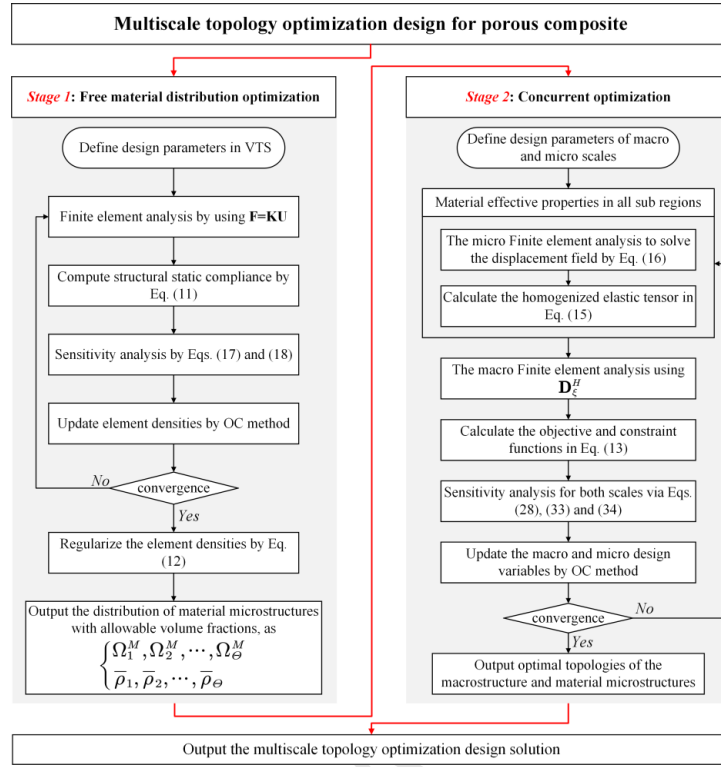
Fig. 4. The flowchart of multiscale topology optimization for porous composites

6. Numerical Examples

In this section, several numerical examples in 2D and 3D are provided to showcase the effectiveness of the multiscale topology optimization method for porous composites. The "ersatz material" model [13] is used to approximately calculate the related properties of those elements cut by the moving boundary in the finite element analysis at two scales. It is known that material microstructures have no specific sizes but should meet the periodic and multiscale conditions to enable the application of the homogenization method [28]. In all examples, the normal sizes of material microstructures are set as 1 mm. The Young's modulus is 210GPa, and the Poisson's ratio is 0.3. In the OC algorithm, the moving limit is $m = 0.002$ and the damping factor is set as 0.3. The termination criteria for the free material distribution optimization is that the difference of the objective values between two successive steps is less than 1e-4, and the concurrent optimization will terminate if the difference is less than 1e-4 or the maximum 200 steps are reached.

6.1 Cantilever beam

In this example, the cantilever beam is used to study the efficiency of the proposed multiscale topology optimization method. As displayed in **Fig. 5**, the beam is fixed along the left side and a force (F=5e5 **N**) is loaded at the middle point of the right side, with the L=1.4m and H=0.7m. The macrostructure is discretized with 140×70 finite elements with four corner nodes, and 80×80 finite elements are used to discretize the microstructures. The dimensions of the macro finite element are equal to 1cm, ten times as the sizes of the microstructures, which can satisfy the conditions of the numerical homogenization to evaluate the effective property of the microstructures. The maximum volume fractions V_M and V_d are defined as 32% and 50%, respectively.
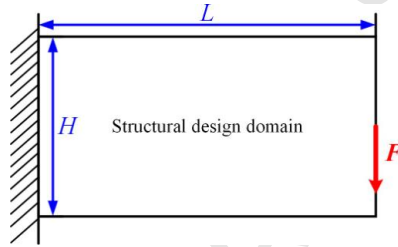
Fig. 5. Cantilever beam

6.1.1 Multiscale design of the cantilever beam

(*a*) *Free* m*aterial distribution optimization*

The distribution of the element densities by the VTS method is displayed in **Fig. 6**. It can be seen that the optimized element densities ranging from 0 to 1 are distributed in an element-wise pattern, where the right-side color bar indicates the element densities. A number of intermediate densities, which corresponds to the microstructures to be designed in the latter concurrent design, are existed in the macrostructure as shown in **Fig. 6**. As mentioned in Section 3.1, in practice it is computationally prohibitive to design all the microstructures relevant to all the elements due to the large number of finite elements.
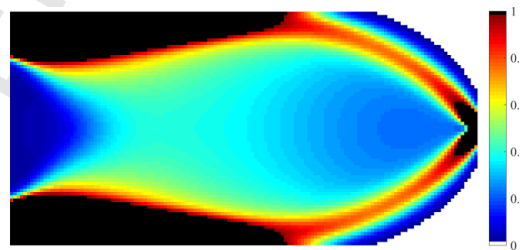

Fig. 6. The distribution of the element densities

Table 1 lists a scheme (**S1**) of the regularization mechanism with the defined thresholds. At the same time, it is assumed that the regularized element densities will be 0 if they are located between 0.0 and 0.2,

17

and the regularized element densities will be 1 if they are within 0.8-1.0, and the intermediate densities are regularized based on Eq. (12). As given in **Fig. 7**, the number of the distinct densities is reduced to 5, and the number of the intermediate densities after regularization is equal to 3. Then, the macro design domain is divided into five sub regions plotted with different colors (white, blue, green, red and black), and each of them is uniformly arranged by a number of identical element densities. In this way, each sub macro domain is occupied by a representative material microstructure. It should be noted that the regularized discrete densities are chosen as the material volume constraints for the corresponding microstructures to be devised in the latter concurrent topology optimization.

Table 1. Scheme 1 (**S1**) of the regularization mechanism

Scheme	The defined thresholds in different groups				
	Group 1	Group 2	Group 3	Group 4	Group 5
S1	$[\rho_{\min}\ \ 0.2)$	$[0.2\ \ 0.4)$	$[0.4\ \ 0.6)$	$[0.6\ \ 0.8)$	$[0.8\ \ 1]$
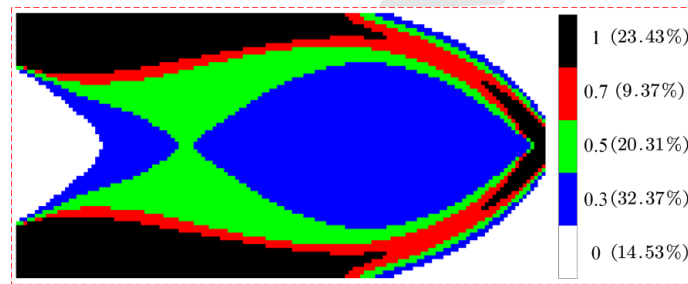
Fig. 7. The regularized distribution of the element densities

(*b*) *Concurrent topology optimization*

The topology of the macrostructure and topologies of five representative microstructures are concurrently optimized, in terms of the overall distribution of these five microstructures in the macro domain in **Fig. 7**. The initial design of the macrostructure is given in **Fig. 8** (*a*). The optimizations for five representative microstructures employ the same initial design, defined in **Fig. 8** (*b*). **Fig. 9** gives the optimized topology of the macrostructure. **Table 2** shows the details of four microstructures (excluding the microstructure with the void), including the optimized micro topologies and the 10×10 repetitive microstructures, as well as the corresponding effective elastic tensors after the homogenization.
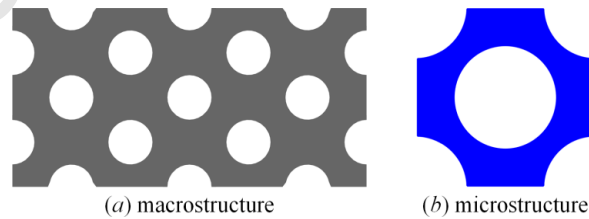

(*a*) macrostructure   (*b*) microstructure

Fig. 8. Initial designs at two scales

18

Fig. 9. The optimized topology of the macrostructure

Table 2. The optimized results of four material microstructures

No	Vol	Microstructure	10×10 repetitive microstructures	Homogenized elastic tensor
2	30%			$\begin{bmatrix} 2.04 & 1.88 & 0 \\ 1.88 & 2.08 & 0 \\ 0 & 0 & 1.67 \end{bmatrix} e^{10}$
3	50%			$\begin{bmatrix} 4.84 & 3.28 & 0 \\ 3.28 & 4.19 & 0 \\ 0 & 0 & 2.89 \end{bmatrix} e^{10}$
4	70%			$\begin{bmatrix} 12.4 & 3.42 & 0 \\ 3.42 & 5.64 & 0 \\ 0 & 0 & 3.74 \end{bmatrix} e^{10}$
5	100%			$\begin{bmatrix} 23.1 & 6.9 & 0 \\ 6.9 & 23.1 & 0 \\ 0 & 0 & 8.1 \end{bmatrix} e^{10}$

In **Fig. 10**, the final multiscale design of the cantilever beam is provided. It can be found that the optimized topology of the macrostructure comprises five different sub domains plotted by different colors (white, blue, green, red and black). Each sub domain is periodically configured by the corresponding representative microstructure with the same color. The topologies of the macrostructure and multiple microstructures are optimized concurrently, and the representative microstructures are appropriately distributed in the design domain. From the results, it can be seen that the microstructure 2 is featured with a geometry via a combination of four bar-style members, which roughly align with the principal stress directions of the material to make the microstructure stretched as much as possible in order to supply the

19

maximal stiffness. When the material volumes become larger such as the microstructures 3 and 4, the overall geometries of the topological designs still bear similarity, but the four members within the microstructures are getting complex and they are no longer bar-style members.
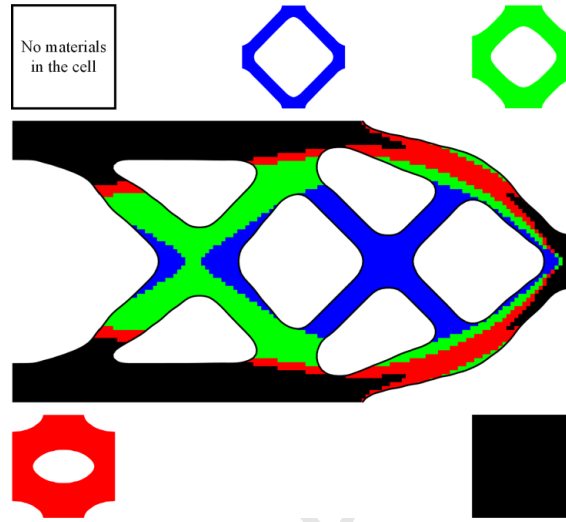

Fig. 10. Multiscale design 1 of the cantilever beam

Furthermore, it is noted that the connectivity between different microstructures can roughly be kept due to the fact that the microstructures have similar topologies at the interfaces of two different microstructures. This phenomenon also complies with the fact that the topology optimization for stiffness design should maintain the connectivity of loading propagation in the macro design domain [45], under the given supports and loading conditions. Finally, it can be found that the optimized topologies at two scales are all featured with the smooth boundaries. Hence, the proposed formulation can fully make use of the favorable features of the VTS method and the PLSM.

(*a*) The objective and the total volume fraction

(*b*) The volume fractions of five microstructures
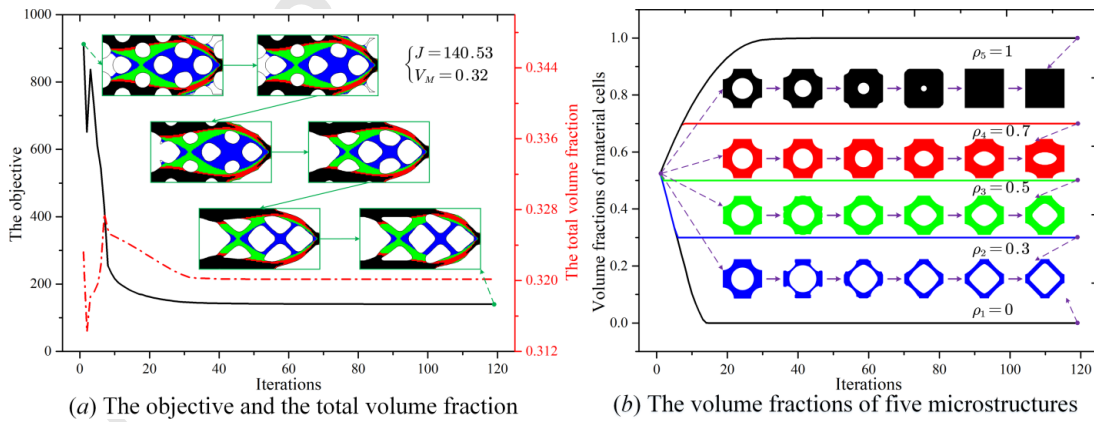
Fig. 11. Iteration histories

20

The convergent histories are displayed in **Fig. 11**, in which the structural mean compliance and the total volume fraction are shown in **Fig. 11** (*a*). The iterations of volume fractions for five representative material microstructures are illustrated in **Fig. 11** (*b*). It can be seen that the iterations are smooth and fast, which shows that the proposed multiscale design method has a high optimization efficiency. The multiscale design optimization remarkably reduces the number of microstructures to be designed, and the PLSM removes several strict numerical implementations in most conventional LSMs.

6.1.2 Influence of the regularization mechanism

In order to address the influence of the free material distribution optimization on the structural performance, we define four regularization schemes (**S2**-**S5**) in **Table 3**. All the design parameters keep the same as Section 6.1.1. The defined four schemes are applied to regularize the element densities in **Fig. 6**, and we can achieve four different regularized distributions presented in **Fig. 12**. Similar to **Fig. 7**, the regularized element densities are distributed in a multi-domain pattern. Meanwhile, the macrostructure is divided into more sub domains, subject to a finer regularization of the continuous distribution of element densities. Hence, four overall distributions of the representative microstructures with allowable volume fractions to be designed are obtained for the latter concurrent topology optimization.
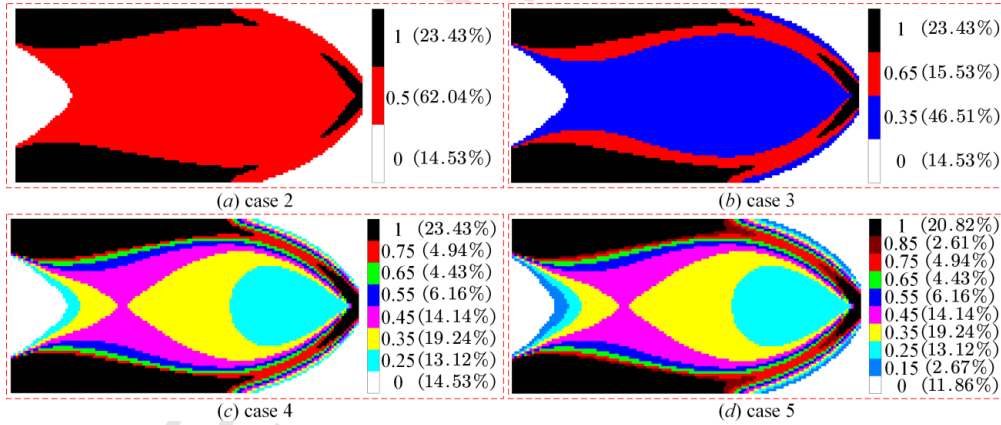

Fig. 12. Four regularized distributions of the element densities

Table 3. Four schemes (**S2**-**S5**) of the regularization mechanism

S2 $[\rho_{\min}\ 0.2),\ [0.2\ 0.8),\ [0.8\ 1];$ **S3** $[\rho_{\min}\ 0.2),\ [0.2\ 0.5),\ [0.5\ 0.8),\ [0.8\ 1];$	
S4 $[\rho_{\min}\ 0.2),\ [0.2\ 0.3),\ [0.3\ 0.4),\ [0.4\ 0.5),\ [0.5\ 0.6),\ [0.6\ 0.7),\ [0.7\ 0.8),\ [0.8\ 1];$	
S5 $[\rho_{\min}\ 0.1),\ [0.1\ 0.2),\ [0.2\ 0.3),\ [0.3\ 0.4),\ [0.4\ 0.5),\ [0.5\ 0.6),\ [0.6\ 0.7),$ $[0.7\ 0.8),\ [0.8\ 0.9),\ [0.8\ 1];$	

The concurrent design for the topology of the macrostructure and the topologies of multiple microstructures are performed in four cases under four different distributions of the representative

21

microstructures. Hence, four different multiscale designs are presented in **Fig. 13**. Similar to the design in **Fig. 10**, all the optimized macro topologies of the multiscale designs in four cases are within different sub domains plotted by different colors. Each of the representative microstructures is uniformly arranged in the corresponding sub domain, which are plotted with the same color. Hence, the effectiveness of the proposed multiscale topology optimization design method for porous composites is further demonstrated.
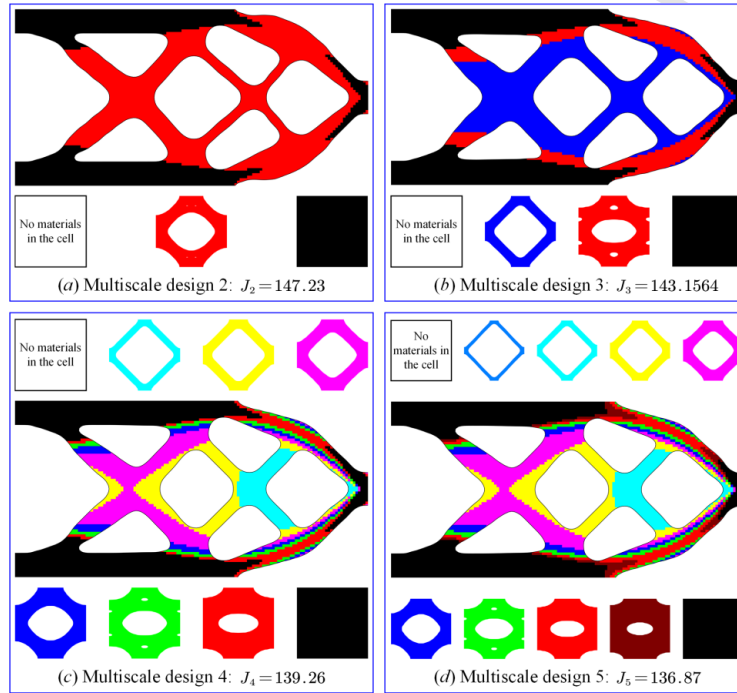
Fig. 13. Multiscale designs of the cantilever beam under four different schemes

Moreover, the optimized objectives in four multiscale designs gradually decrease with the increasing of the number of the representative microstructures, as $J_2 > J_3 > J_4 > J_5$. The main reason is that a finer regularization generates a finer distribution of multiple representative microstructures in the macrostructure, so that the design freedom of the structural performance is expanded [45,50]. In **Fig. 13** (*d*), it is noted that the final multiscale design 5 does not comprise the microstructure 2 with the volume fraction 15%. It may be because the microstructure 2 contributes less to improve the overall stiffness for the macrostructure, and it is not included in the final design. In this way, we may conclude that when the types of the microstructures reach to a certain number, a further increase of their diversity cannot lift the performance of the macro structure.

6.1.3 Influence of the symmetry condition

22

In this subsection, we will study the influence of the symmetry condition on the structural performance. All the design parameters are consistent with Section 6.1.1. The **S1** scheme of the regularization mechanism is used to reduce the number of the intermediate densities. The regularized distribution should be same as **Fig. 7**. However, in order to remove the effect of the symmetry of the macro loads and boundary conditions on the optimization of the microstructures, we partition the regularized distribution along the transverse central axis of the cantilever beam. The final distribution is shown in **Fig. 14**. It can be seen that the macrostructure is divided into eight sub domains.
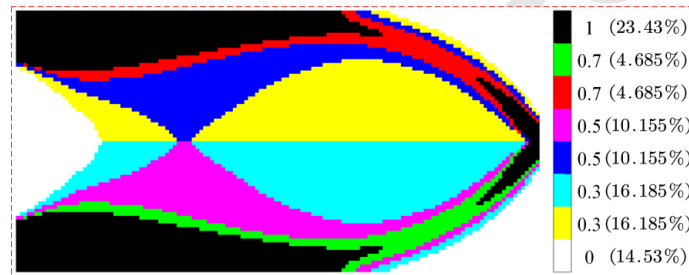
Fig. 14. The regularized distribution

The concurrent optimization for the macrostructure and microstructures is performed, subject to the overall distribution of multiple microstructures shown in **Fig. 14**. The final multiscale design of the cantilever beam without the symmetry condition imposing on the optimization of microstructures is displayed in **Fig. 15**. It can be seen that the microstructures are both featured with the anisotropic (excluding the microstructures with full solid and void). The optimized structural compliance J_6 is less than the objective J_1 in Subsection 6.1.1. Hence, the structural stiffness is further improved. It shows that the anisotropic microstructures are beneficial to the enhancement of the performance, mainly because the symmetric condition imposed on the optimization of material microstructures limits the design flexibility to improve the structure performance.
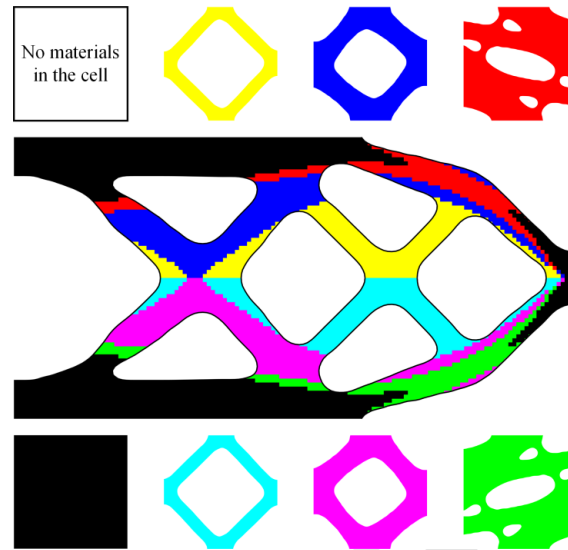
23

Fig. 15. Multiscale design of the cantilever beam: J_6=130.62

6.1.4 Comparison with conventional multiscale design

To display the positive features of the proposed multiscale design, the cantilever beam is optimized by the conventional multiscale design [38,40] that the identical microstructure is uniformly and periodically arrayed within the macrostructure. It is noted that the concurrent topology optimization formulation in this paper will be degraded to the conventional multiscale design, if the distribution only contains a number of identical microstructures. The design parameters are consistent with those given in Section 6.1.1.

The final multiscale topology optimization design in shown in **Fig. 16**, and the objective value is J_0=207.96. Hence, it can be seen that the optimized structural performance by the proposed multiscale design is much better than the conventional multiscale design (J_0>J_2>J_3>J_1>J_4>J_5), which shows the benefit of the current multiscale topology optimization method. The free material distribution optimization can guide an adaptive configuration of the microstructures in the macrostructure for the enhancement of the performance.
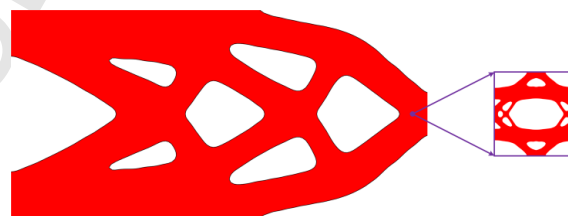

Fig. 16. Conventional multiscale design: J_0=207.96

6.2 Michell structure

24

In this example, we further study the efficiency of the proposed multiscale topology optimization method. The Michell structure (**Fig. 17**) is loaded with a concentrated vertical force (F=1e6 **N**) at the center of the bottom edge. The bottom-left corner is fixed and the bottom-right corner is supported on a roller. The structural sizes are defined with L=1.6 m and H=0.8 m. The macrostructure is discretized by a mesh of 160×80 finite elements, and a mesh of 80×80 finite elements is used to discretize the microstructures. The ratio between the dimensions of microstructures and macro finite elements is equal to 0.1, which means one finite element consists of a pattern of 10×10=100 microstructures, to improve the numerical accuracy. The maximum volume fractions V_M and V_d in the design are 0.26 and 0.5, respectively.
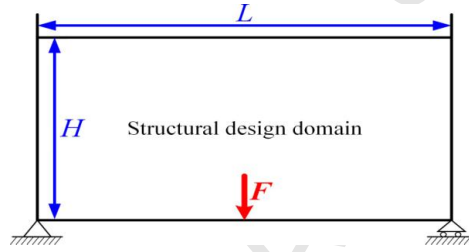
Fig. 17. Michell structure

6.2.1 Free material distribution optimization

In the distribution optimization, we firstly employ the VTS method to optimize the element densities, which is shown in **Fig. 18** (*a*). The element densities are continuously varied from 0 to 1 in the macrostructure, which leads to a large amount of microstructures to design. We use the **S1** scheme in **Table 1** to regularize the continuously distributed element densities. Meanwhile, the symmetry of the macro loads and boundary conditions on the design of multiple microstructures is not considered. Without the consideration of the symmetry may improve the stiffness of the structure. Hence, the overall distribution of the regularized element densities is partitioned along the vertical axis, as illustrated in **Fig. 18**(*b*). It can be seen that the element densities also distribute in a domain-wise pattern, also similar to the results in Section 6.1.
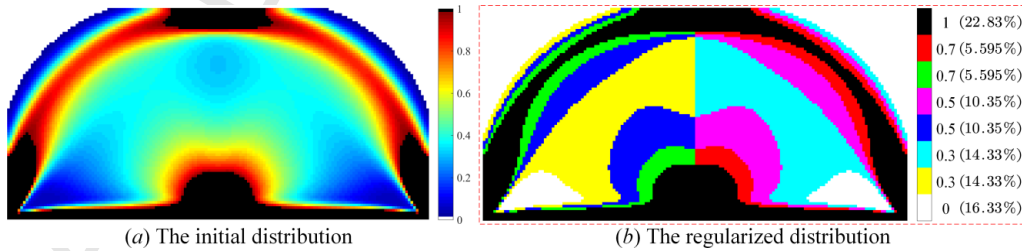
(*a*) The initial distribution   (*b*) The regularized distribution

Fig. 18. Two distributions

25

6.2.2 Concurrent topology optimization

The topology of the macrostructure and topologies of multiple microstructures are concurrently optimized, subject to the overall distribution gained in **Fig. 18** (*b*). The initial design of the macrostructure is defined in **Fig. 19** (*a*). The designs for multiple representative microstructures start from the same initial guesses displayed in **Fig. 19** (*b*), due to the topologies of microstructures not known. The optimized topology of the macrostructure is shown in **Fig. 20**. The optimized results of representative microstructures (excluding the microstructures with void) are clearly listed in **Table 4**, including the optimized topology, 10×10=100 repetitive microstructures, and the corresponding homogenized elastic tensors. In **Table 4**, the material microstructures 2, 4, and 6 are symmetric with respect to the microstructures 3, 5, 7, respectively. It can also be seen from the effective elastic tensors of the microstructures after homogenization.
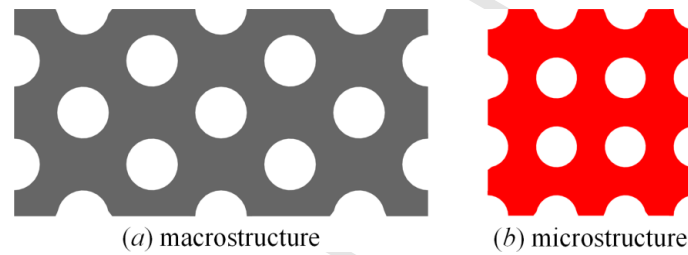
(*a*) macrostructure   (*b*) microstructure
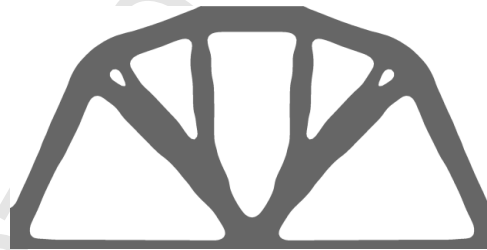
Fig. 19. Initial designs at two scales
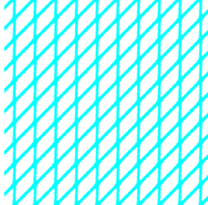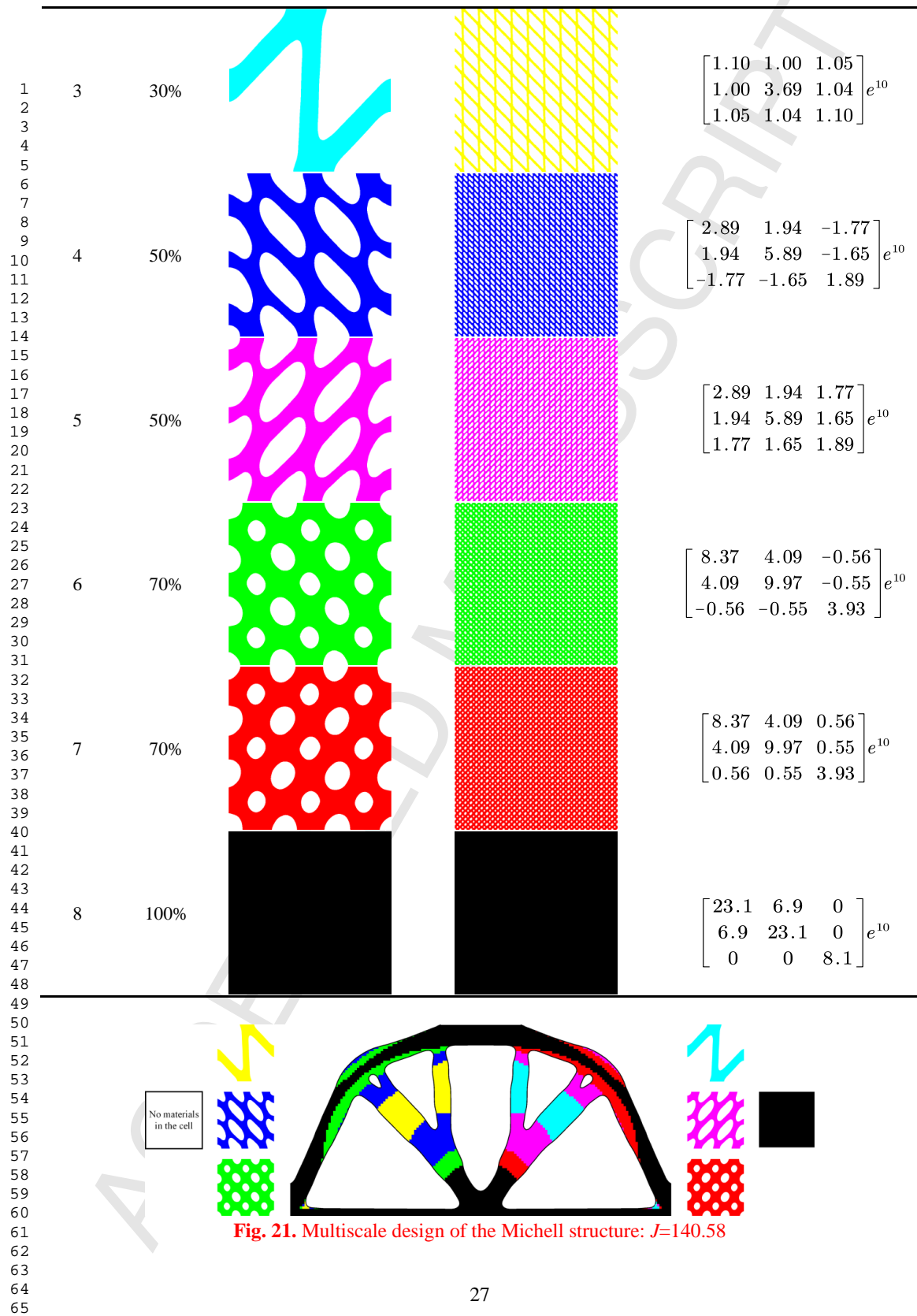
Fig. 20. The optimized topology of the macrostructure

Table 4. The optimized numerical results of material microstructures

Order	Vol	Microstructure	10×10 repetitive microstructures	Homogenized elastic tensor
2	30%			$\begin{bmatrix} 1.10 & 1.00 & -1.05 \\ 1.00 & 3.69 & -1.04 \\ -1.05 & -1.04 & 1.10 \end{bmatrix} e^{10}$

26

3	30%			$\begin{bmatrix} 1.10 & 1.00 & 1.05 \\ 1.00 & 3.69 & 1.04 \\ 1.05 & 1.04 & 1.10 \end{bmatrix} e^{10}$
4	50%			$\begin{bmatrix} 2.89 & 1.94 & -1.77 \\ 1.94 & 5.89 & -1.65 \\ -1.77 & -1.65 & 1.89 \end{bmatrix} e^{10}$
5	50%			$\begin{bmatrix} 2.89 & 1.94 & 1.77 \\ 1.94 & 5.89 & 1.65 \\ 1.77 & 1.65 & 1.89 \end{bmatrix} e^{10}$
6	70%			$\begin{bmatrix} 8.37 & 4.09 & -0.56 \\ 4.09 & 9.97 & -0.55 \\ -0.56 & -0.55 & 3.93 \end{bmatrix} e^{10}$
7	70%			$\begin{bmatrix} 8.37 & 4.09 & 0.56 \\ 4.09 & 9.97 & 0.55 \\ 0.56 & 0.55 & 3.93 \end{bmatrix} e^{10}$
8	100%			$\begin{bmatrix} 23.1 & 6.9 & 0 \\ 6.9 & 23.1 & 0 \\ 0 & 0 & 8.1 \end{bmatrix} e^{10}$

No materials in the cell

Fig. 21. Multiscale design of the Michell structure: J=140.58

27

The optimized multiscale design of the Michell structure is provided in **Fig. 21**. It is noted that the microstructures with solid and void are excluded in the final design to simplify the description. We can see that the optimized topology of the macrostructure consists of eight sub domains, indicated by eight colors. Each sub domain is periodically distributed by the corresponding representative microstructure. Hence, the effectiveness of the proposed multiscale method considering three design elements is further demonstrated. Additionally, it can be seen that the upper and lower edges of the Michell structure are occupied by the solid microstructures, in order to provide the sufficient stiffness and limit bending deformation in the Michell structure. It is also noticed that the connectivity of microstructures is basically maintained in the macro domain to ensure a reasonable macroscopic response [45].

6.3 3D supported structure

In this example, we study the effectiveness of the proposed multiscale optimization method on 3D porous composites. A 3D supported structure is given in **Fig. 22**, which is fixed at four corners in the bottom surface and loaded with a force (F=1e7 **N**) at the middle of the top surface. The sizes of the design domain are L=0.2m, W=0.2m and H=0.15m. The macrostructure is discretized by $20\times20\times15$ finite elements, and a mesh of $15\times15\times15$ finite elements is used to discretize microstructures. It is also noted that the ratio between the sizes of microstructures and macro finite elements is equal to 0.1, which indicates that a macro finite element consists of $10\times10\times10$=1000 microstructures. The allowable volume fractions V_M and V_d in the multiscale topology optimization formulation are set to 30% and 50%, respectively.
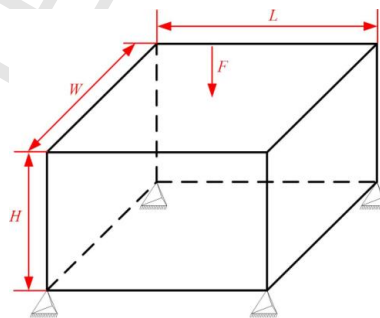

Fig. 22. 3D supported structure

6.3.1 Free material distribution optimization

In the distribution optimization, the distribution of the element densities optimized by the VTS method is illustrated in **Fig. 23** (*a*), where a large number of the intermediate element densities are distributed in the domain. We still adopt the **S1** scheme in **Table 1** to regularize the element densities, and the regularized

28

distribution is shown in **Fig. 23** (*b*). We also give the cross-sectional view of the regularized distribution to display the interior of the macrostructure.
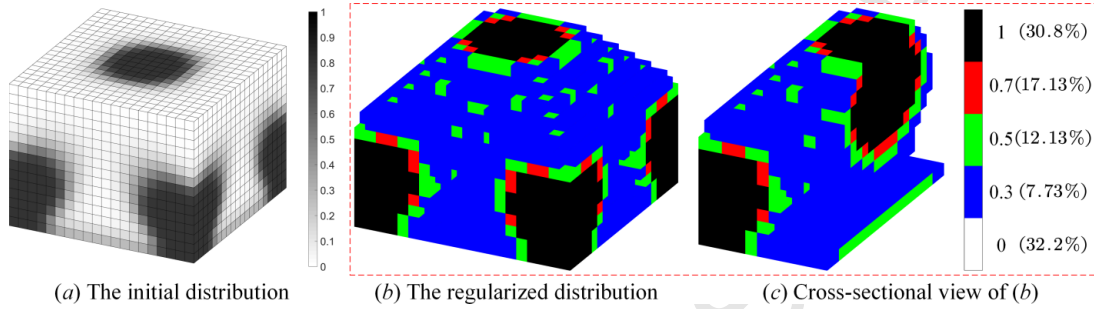

(*a*) The initial distribution   (*b*) The regularized distribution   (*c*) Cross-sectional view of (*b*)

Fig. 23. Two distributions

6.3.2 Concurrent topology optimization

The concurrent optimization for the topologies of both the macrostructure and multiple microstructures is performed. The initial designs at two scales are defined in **Fig. 24**, and five microstructures from the same initial design are displayed in **Fig. 24** (*b*). The optimized macro topology is illustrated in **Fig. 25**, and the optimized topologies of four representative microstructures (excluding the microstructure with void) are, respectively, listed in the third column of **Table 5**. Moreover, the cross-sectional views of the representative microstructures are also provided, to present the detailed geometrical features. 10×10×10 repetitive material microstructures are also listed in **Table 5**.

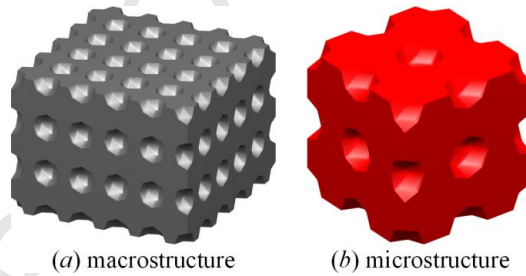
(*a*) macrostructure   (*b*) microstructure

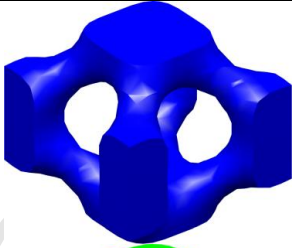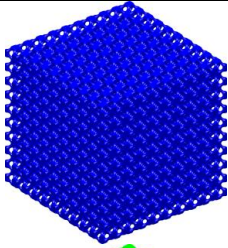**Fig. 24.** Initializations of the macrostructure and material microstructures
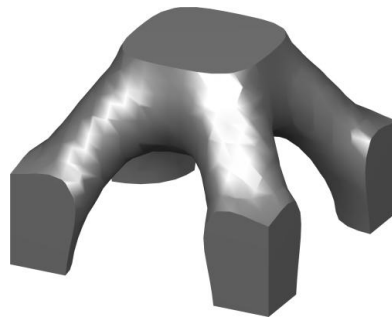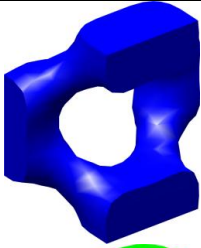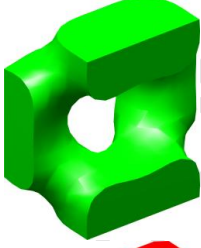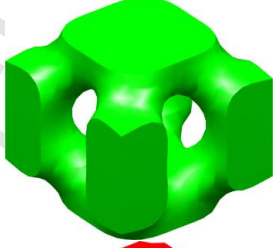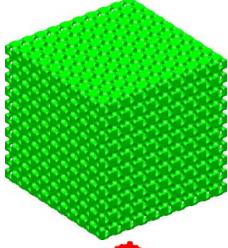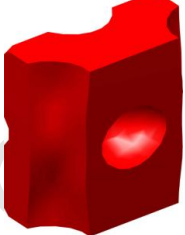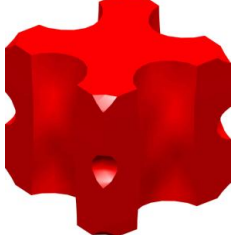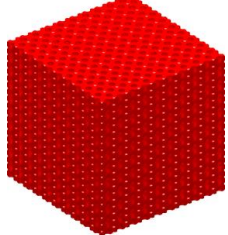

Fig. 25. The optimized topology of the macrostructure.

29

The final multiscale design of the 3D supported structure is displayed in **Fig. 26**, where the macrostructure comprises five representative microstructrues indicated by five different colors (white, blue, green, red and black). Each material mcirostructure is uniformly distributed in its corresponding sub domain, which are plotted with the same color. Hence, each macro sub domain is featured with a unique macroscopic effective property. The optimization of 3D composites considering from three design pillars further demonstrates the effectiveness of the proposed multiscale design method. It can be seen that the sub domains plotted by the green and the red is smaller than the sub area plotted with the blue. However, it is noted that the periodic condition of the homogenization method to evaluate the macroscopic effective properties is roughly met and the numerical accuracy is slightly improved, as each macro element contains 1000 microstructures. The sizes of the microstructures are then much smaller than that of macro finite elements.

Table 5. The optimized numerical results of material microstructures

Order	Vol	Cross-sectional view	Microstructure	10×10×10 repetitive microstructures
2	30%			
3	50%			
4	70%			

5   100%

No materials
in the cell

$1\times1\times1$ $10\times10\times10$

$1\times1\times1$ $10\times10\times10$

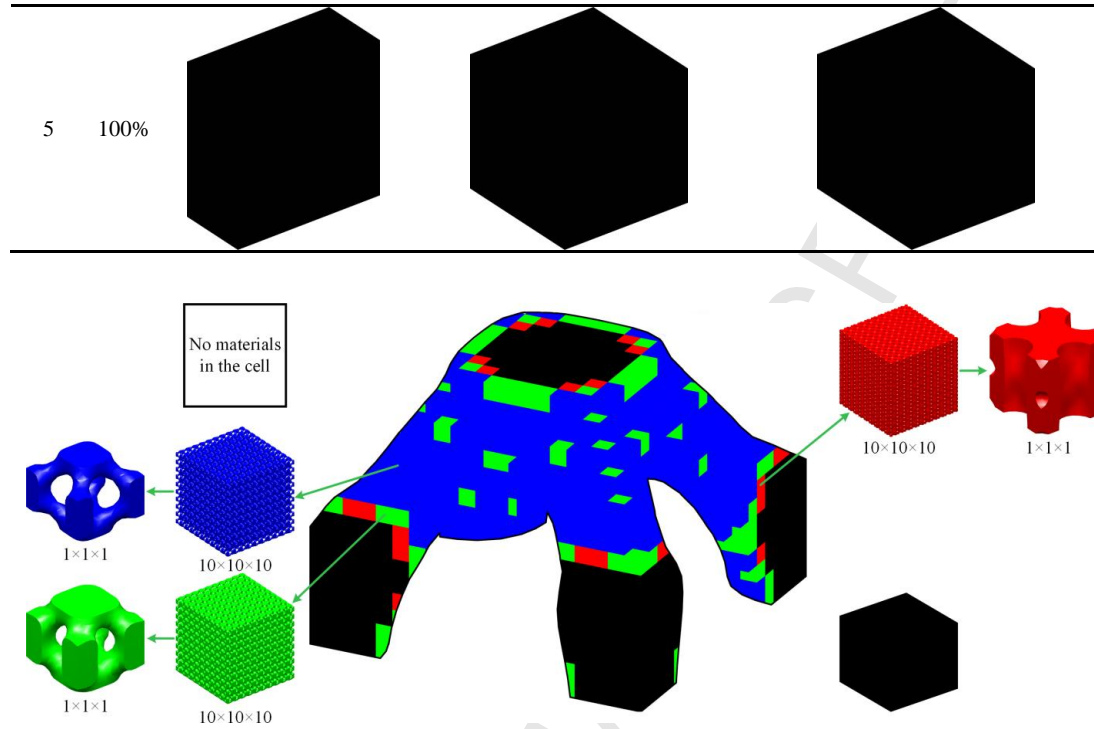$10\times10\times10$ $1\times1\times1$

Fig. 26. Multiscale design of the 3D supported structure

Meanwhile, the convergent histories of the optimized objective and volume fractions for the macro structure are shown in **Fig. 27** (*a*), and some typical intermediate designs at micro scale are also presented in **Fig. 27** (*b*). The iterative curves show that the topologies of the designs can converge within the first 20 steps and then the afterwards iterations are used to implement shape variations.

$\begin{cases} J_1 = 3.83 \\ V_M = 0.3 \end{cases}$

(*a*) The objective and the total volume fraction

$\rho_5 = 1$

$\rho_4 = 0.7$

$\rho_3 = 0.5$

$\rho_2 = 0.3$

$\rho_1 = 0$

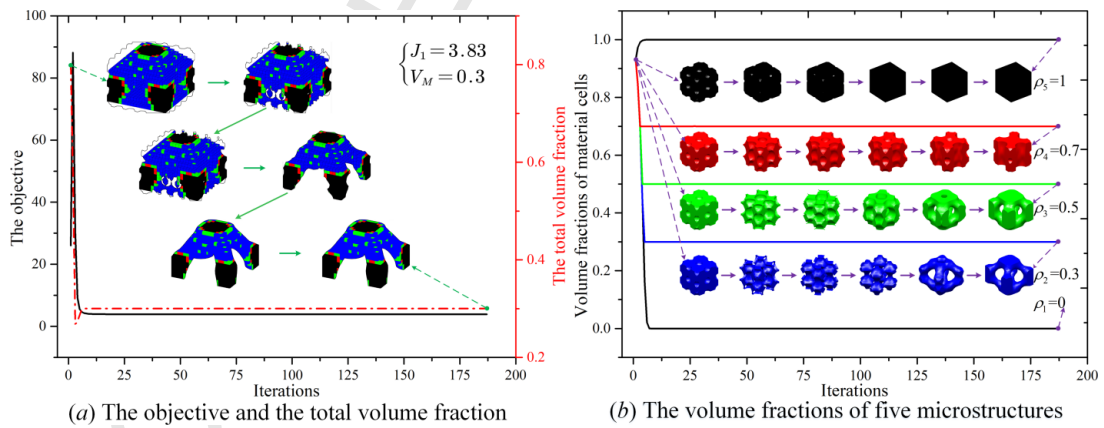(*b*) The volume fractions of five microstructures

Fig. 27. Evolution histories

31

7 Conclusions

In this paper, we propose an effective multiscale topology optimization method for design of porous composites with the multi-domain microstructures, by considering the topology of the macrostructure, the topologies of microstructures and their overall distribution. The optimization mainly involves two stages, namely the free material distribution optimization and the concurrent topology optimization. The former stage obtained by the VTS method together with a regularization mechanism is used to generate a discrete distribution of the microstructures in the macro design domain. The latter stage is to concurrently optimize the topologies of both the macrostructure and multiple microstructures, based on the distribution of the microstructures achieved in the previous stage. Several examples have been used to show the effectiveness of the proposed multiscale design method. The optimized topology of the macrostructure in the multiscale design is divided into multiple sub domains and each of sub macro domain is uniformly configured by the corresponding representative microstructure. The number of the representative microstructures has an effect on the improvement of the structural stiffness. Numerical results denote that the macro loads and boundary conditions play a critical role in the design for the topologies of microstructures. The symmetrical condition on the macro structure also has an impact on the designs of the multiscale topology optimization.

Acknowledgments

References

[1]   L.J. Gibson, M.F. Ashby, Cellular solids: structure and properties, Cambridge university press, 1999.

[2]   R.M. Christensen, Mechanics of cellular and other low-density materials, Int. J. Solids Struct. 37 (2000) 93–104.

[3]   H. Masuda, K. Fukuda, Ordered metal nanohole arrays made by a two-step replication of honeycomb structures of anodic alumina, Science. 268 (1995) 1466–1468.

[4]   D. Wang, Impact behavior and energy absorption of paper honeycomb sandwich panels, Int. J. Impact Eng. 36 (2009) 110–114.

[5]   M.P. Bendsøe, O. Sigmund, Topology Optimization: Theory, Methods, and Applications, Springer, Berlin, Heidelberg, 2003.

[6]   O. Sigmund, K. Maute, Topology optimization approaches, Struct. Multidiscip. Optim. 48 (2013) 1031–1055.

32

[7]   M. Bendsoe, N. Kikuchi, Generating optimal topologies in stuctural design using a homogenization method, Comput Methods Appl Mech Eng. 71 (1998) 197–224.

[8]   M. Zhou, G.I.N. Rozvany, The COC algorithm, Part II: Topological, geometrical and generalized shape optimization, Comput. Methods Appl. Mech. Eng. 89 (1991) 309–336.

[9]   M.P. Bendsøe, O. Sigmund, Material interpolation schemes in topology optimization, Arch. Appl. Mech. 69 (1999) 635–654.

[10]   Y.M. Xie, G.P. Steven, A simple evolutionary procedurefor structural optimization, Comput. Struct. 49 (1993) 885–969.

[11]   J.A. Sethian, A. Wiegmann, Structural Boundary Design via Level Set and Immersed Interface Methods, J. Comput. Phys. 163 (2000) 489–528.

[12]   M.Y. Wang, X. Wang, D. Guo, A level set method for structural topology optimization, Comput. Methods Appl. Mech. Eng. 192 (2003) 227–246.

[13]   G. Allaire, F. Jouve, A.M. Toader, Structural optimization using sensitivity analysis and a level-set method, J. Comput. Phys. 194 (2004) 363–393.

[14]   Z. Kang, Y. Wang, Structural topology optimization based on non-local Shepard interpolation of density field, Comput. Methods Appl. Mech. Eng. 200 (2011) 3515–3525.

[15]   Z. Luo, N. Zhang, Y. Wang, W. Gao, Topology optimization of structures using meshless density variable approximants, Int. J. Numer. Methods Eng. 93 (2013) 443–464.

[16]   Z. Luo, L. Tong, A level set method for shape and topology optimization of large-displacement compliant

mechanisms, Int. J. Numer. Methods Eng. 76 (2008) 862–892.

[17]   Z. Luo, M. Wang, S. Wang, P. Wei, A level set based parameterization method for structural shape and topology optimization, Int. J. Numer. Methods Eng. 76 (2008) 1–26.

[18]   Q. Xia, M.Y. Wang, S. Wang, S. Chen, Semi-Lagrange method for level-set-based structural topology and shape optimization, Struct. Multidiscip. Optim. 31 (2006) 419–429.

[19]   T. Yamada, K. Izui, S. Nishiwaki, A. Takezawa, A topology optimization method based on the level set method incorporating a fictitious interface energy, Comput. Methods Appl. Mech. Eng. 199 (2010) 2876–2891.

[20]   P.D. Dunning, H. Alicia Kim, A new hole insertion method for level set based structural topology optimization, Int. J. Numer. Methods Eng. 93 (2013) 118–134.

[21]   G.I.N. Rozvany, M.P. Bendsøe, U. Kirsch, Layout optimization of structures, Appl. Mech. Rev. 48 (1995) 41–119.

[22]   K. Svanberg, The method of moving asymptotes - a new method for structural optimization, Int. J. Numer. Methods Eng. 24 (1987) 359–373.

[23]   Y. Wang, Z. Luo, N. Zhang, Z. Kang, Topological shape optimization of microstructural metamaterials using a level set method, Comput. Mater. Sci. 87 (2014) 178–186.

[24]   H. Li, P. Li, L. Gao, L. Zhang, T. Wu, A level set method for topological shape optimization of 3D structures with extrusion constraints, Comput. Methods Appl. Mech. Eng. 283 (2015) 615–635.

[25]   Y. Wang, Z. Luo, Z. Kang, N. Zhang, A multi-material level set-based topology and shape optimization method, Comput. Methods Appl. Mech. Eng. 283 (2015) 1570–1586.

[26]   Y. Wang, J. Gao, Z. Luo, T. Brown, N. Zhang, Level-set topology optimization for multimaterial and multifunctional mechanical metamaterials, Eng. Optim. 49 (2017) 22–42.

[27]   J. Fu, H. Li, M. Xiao, L. Gao, S. Chu, Topology optimization of shell-infill structures using a distance regularized parametric level-set method, Struct. Multidiscip. Optim. (2018). https://doi.org/10.1007/s00158-018-2064-6

[28] J.M. Guedes, N. Kikuchi, Preprocessing and Postprocessing for Materials Based on the Homogenization Method With Adaptive Finite Element Methods, Comput. Methods Appl. Mech. Eng. 83 (1990) 143–198.

[29] O. Sigmund, Materials with prescribed constitutive parameters: An inverse homogenization problem, Int. J. Solids Struct. 31 (1994) 2313–2329.

[30] X. Huang, A. Radman, Y.M. Xie, Topological design of microstructures of cellular materials for maximum bulk or shear modulus, Comput. Mater. Sci. 50 (2011) 1861–1870.

[31] J. Gao, H. Li, L. Gao, M. Xiao, Topological shape optimization of 3D micro-structured materials using energy-based homogenization method, Adv. Eng. Softw. 116 (2018) 89–102.

[32] J.K. Guest, J.H. Prévost, Optimizing multifunctional materials: design of microstructures for maximized stiffness and fluid permeability, Int. J. Solids Struct. 43 (2006) 7028–7047.

[33] V.J. Challis, J.K. Guest, J.F. Grotowski, A.P. Roberts, Computationally generated cross-property bounds for stiffness and fluid permeability using topology optimization, Int. J. Solids Struct. 49 (2012) 3397–3408.

[34] J. Gao, H. Li, Z. Luo, L. Gao, P. Li, Topology optimization of micro-structured materials featured with the specific mechanical properties. (arXiv:1808.08647v1 [cs.CE]), Int. J. Comput. Methods. (2018). doi:10.1142/S021987621850144X.

[35] H. Rodrigues, J.M. Guedes, M.P. Bendsoe, Hierarchical optimization of material and structure, Struct. Multidiscip. Optim. 24 (2002) 1–10.

[36] L. Liu, J. Yan, G. Cheng, Optimum structure with homogeneous optimum truss-like material, Comput. Struct. 86 (2008) 1417–1425.

[37] J. Yan, Z. Duan, E. Lund, J. Wang, Concurrent multi-scale design optimization of composite frames with manufacturing constraints, Struct. Multidiscip. Optim. 56 (2017) 519–533.

[38] Y. Wang, M.Y. Wang, F. Chen, Structure-material integrated design by level sets, Struct. Multidiscip. Optim. 54 (2016) 1145–1156.

[39] J. Kato, D. Yachi, K. Terada, T. Kyoya, Topology optimization of micro-structure for composites applying a decoupling multi-scale analysis, Struct. Multidiscip. Optim. 49 (2014) 595–608.

[40] X. Huang, S.W. Zhou, Y.M. Xie, Q. Li, Topology optimization of microstructures of cellular materials and composites for macrostructures, Comput. Mater. Sci. 67 (2013) 397–407.

[41] B. Niu, J. Yan, G. Cheng, Optimum structure with homogeneous optimum cellular material for maximum fundamental frequency, Struct. Multidiscip. Optim. 39 (2009) 115–132.

[42] L. Xia, P. Breitkopf, Recent Advances on Topology Optimization of Multiscale Nonlinear Structures, Arch. Comput. Methods Eng. 24 (2017) 227–249.

[43] W.H. Zhang, S.P. Sun, Scale-related topology optimization of cellular materials and structures, Int. J. Numer. Methods Eng. 68 (2006) 993–1011.

[44] J. Alexandersen, B.S. Lazarov, Topology optimisation of manufacturable microstructural details without length scale separation using a spectral coarse basis preconditioner, Comput. Methods Appl. Mech. Eng. 290 (2015) 156–182.

[45] H. Li, Z. Luo, N. Zhang, L. Gao, T. Brown, Integrated design of cellular composites using a level-set topology optimization method, Comput. Methods Appl. Mech. Eng. 309 (2016) 453–475.

[46] Y. Zhang, M. Xiao, H. Li, L. Gao, S. Chu, Multiscale concurrent topology optimization for cellular structures with multiple microstructures based on ordered SIMP interpolation, Comput. Mater. Sci. 155 (2018) 74–91.

[47] H. Li, Z. Luo, L. Gao, P. Walker, Topology optimization for functionally graded cellular composites with metamaterials by level sets, Comput. Methods Appl. Mech. Eng. 328 (2018) 340–364.

[48] L. Xia, P. Breitkopf, Concurrent topology optimization design of material and structure within FE 2 nonlinear multiscale analysis framework, Comput. Methods Appl. Mech. Engrg. 278 (2014) 524–542.

[49] L. Xia, P. Breitkopf, Multiscale structural topology optimization with an approximate constitutive model for local material microstructure, Comput. Methods Appl. Mech. Eng. 286 (2015) 147–167.

[50] Y. Wang, F. Chen, M.Y. Wang, Concurrent design with connectable graded microstructures, Comput. Methods Appl. Mech. Eng. 317 (2017) 84–101.

[51] Y. Wang, L. Zhang, S. Daynes, H. Zhang, S. Feih, M.Y. Wang, Design of graded lattice strucutre with optimized mesostructures for additve manufacturing, Mater. Des. 142 (2018) 114–123.

[52] H. Li, Z. Luo, L. Gao, Q. Qin, Topology optimization for functionally graded cellular composites with multi-patch microstructures by level sets, Comput. Methods Appl. Mech. Eng. 328 (2018) 340–364.

[53] J.P. Groen, O. Sigmund, Homogenization-based topology optimization for high-resolution manufacturable microstructures, Int. J. Numer. Methods Eng. 113 (2018) 1148–1163.

[54] R. Sivapuram, P.D. Dunning, H.A. Kim, Simultaneous material and structural optimization by multiscale topology optimization, Struct. Multidiscip. Optim. 54 (2016) 1267–1281.

[55] L. Xu, G. Cheng, Two-scale concurrent topology optimization with multiple micro materials based on principal stress orientation, Adv. Struct. Multidiscip. Optim. 57 (2018) 2093–2107.

[56] O. Sigmund, N. Aage, E. Andreassen, On the (non-) optimality of Michell structures, Struct. Multidiscip. Optim. 54 (2016) 361–373.

[57] H. Wendland, Piecewise polynomial, positive definite and compactly supported radial functions of minimal degree, Adv. Comput. Math. 4 (1995) 389–396.

[58] S. Osher, R. Fedkiw, Level set methods and dynamic implicit surfaces, Springer Science & Business Media, 2006.

[59] K.K. Choi, N.-H. Kim, Structural sensitivity analysis and optimization 1: linear systems, Springer Science & Business Media, 2006.